Journal of Materials Chemistry A

ROYAL SOCIETY OF CHEMISTRY

PAPER

View Article Online
View Journal | View Issue

Cite this: J. Mater. Chem. A, 2025, 13, 4908

Alloy nanocluster artificial photosystems steering photoredox organic transformation†

Bing-Xiong Zheng,[a] Jiao-Nan Yuan,[a] Peng Su,[a] Xian Yan,[a] Qing Chen,[a] Meng Yuan[a] and Fang-Xing Xiao *[ab]

Atomically precise alloy nanoclusters (NCs) represent an emerging sector of metal nanomaterials as a new generation of photosensitizers for light harvesting and conversion, owing to their distinctive atom-stacking pattern, quantum confinement effect, and enriched active sites. Despite the sporadic progress made in the past few years in constructing alloy NCs photosystems, photoinduced charge transfer characteristics and photocatalytic mechanisms of alloy NCs still remain elusive. In this work, we conceptually demonstrate the rational design of alloy NC ($Au_{1-x}Ag_x$, $Au_{1-x}Pt_x$, and $Au_{1-x}Cu_x$)/transition metal chalcogenide (TMCs) heterostructure photosystems *via* a ligand-triggered self-assembly strategy. The results signify that electrons photoexcited in alloy NCs can smoothly transport to the TMC substrate with the aid of an intermediate ultrathin organic molecule layer, while holes migrate in the opposite direction, promoting the charge separation and prolonging the charge lifetime. Benefitting from the advantageous charge migration, the self-assembled alloy NC/TMC heterostructures exhibit significantly enhanced photoactivity towards selective photoredox organic transformation including selective reduction of aromatic nitro compounds to amino derivatives and selective oxidation of aromatic alcohols to aldehydes under visible light. The predominant active species during the photoredox catalysis are determined, through which alloy NC-dominated photoredox mechanisms are elucidated. Our work provides new insights into the smart construction of atomically precise alloy NC hybrid photosystems, and more importantly, paves the way for regulating the spatially vectorial charge transfer over alloy NCs to achieve solar-to-chemical energy conversion.

Received 25th November 2024
Accepted 8th January 2025

DOI: 10.1039/d4ta08327j

rsc.li/materials-a

1. Introduction

Metal nanoclusters (NCs) with a precise number of metal atoms and ligands (<2 nm in size) have been attracting immense attention in recent years due to their distinctive atom-stacking pattern, quantum confinement effect, and abundant catalytic active sites, representing an emerging sector of metal materials.[1–4] Most intriguingly, metal NCs exhibit favorable highest occupied molecular orbital–lowest unoccupied molecular orbital (HOMO–LUMO) gaps by virtue of their discrete energy band structure featuring the potential to serve as high-efficiency photosensitizers.[5–7] Despite these advantages, due to the ultra-high surface energy caused by their ultra-small particle size, atomically precise metal NCs inevitably suffer from photo/thermal-induced oxidative aggregation, leading to poor stability and unsatisfactory photosensitization effects, thus hindering the widespread application of metal NC photosystems.[8–11] Therefore, searching for applicable strategies to effectively tackle these challenges is of paramount significance to take full advantage of the generic merits of metal NCs and push forward the development of metal NC photocatalysis.

Despite the sporadic investigations reported on the photocatalysis of metal NC/semiconductor photosystems, the ultrafast charge recombination rate and inherent instability of metal NCs remarkably retard the exploration of metal NCs photosystems.[12–15] To surmount the obstacles, several key issues should be rationally considered including (1) the integration mode between metal NCs and semiconductors should be precisely customized for fine tuning of the interface configuration; (2) a close interface is essential to ensure the highly efficient interfacial charge transfer between metal NCs and semiconductors; (3) controllable charge transport over metal NCs is the premise for facilitating charge separation. To date, considerable attention has been focused on unraveling the emerging potential of metal NCs as photosensitizers for stimulating light harvesting and charge migration, but predominant metal NCs are restricted to conventional homo-atomic metal NCs, leaving the construction of alloy NC photosystems in the infancy stage because of the difficulty in synthesizing alloy NCs

[a]College of Materials Science and Engineering, Fuzhou University, New Campus, Minhou, Fujian Province, 350108, China

[b]State Key Laboratory of Structural Chemistry, Fujian Institute of Research on the Structure of Matter, Chinese Academy of Sciences, Fuzhou, Fujian, 350002, P. R. China. E-mail: fxxiao@fzu.edu.cn

† Electronic supplementary information (ESI) available. See DOI: https://doi.org/10.1039/d4ta08327j

and our confined understanding of charge transport characteristics of alloy NCs.[16–21] Doping heteroatoms into homoatomic metal NCs represents a feasible approach to attain the precise control of physicochemical properties and thermodynamic stability of metal NCs.[22] It is well established that doping foreign atoms into parent metal NCs can effectively enhance the thermal stability and catalytic activity through favorable electronic structure modulation.[23,24] Consequently, we deduce that the drawbacks of monometallic NCs such as instability and ultra-short carrier lifetime could be overcome by crafting robust alloy NCs, and simultaneously the generic advantageous photosensitization effects of metal NCs are maintained, through which the diversity of photosensitive metal NCs will be significantly enriched.[25]

Herein, we conceptually demonstrate the construction of alloy NCs/transition metal chalcogenide (TMCs) artificial photosystems, in which atomically precise glutathione (GSH)-protected alloy NCs ($Au_{1-x}Ag_x$, $Au_{1-x}Pt_x$, and $Au_{1-x}Cu_x$) are uniformly and intimately grafted on the TMC substrate *via* an electrostatic self-assembly approach under ambient conditions. The mercaptoethylamine (MEA) molecules anchored on the CdS framework function as interfacial charge transfer mediators to promote the directional charge migration between TMC (CdS) and alloy NCs. We ascertain that electron transfer from the LUMO level of alloy NCs to the conduction band (CB) of TMC (CdS), with holes flowing in the opposite direction, thereby significantly prolonging the carrier lifetime of alloy NCs. Benefiting from the advantageous charge transfer, the self-assembled metal NC/TMC heterostructures exhibit considerably enhanced visible-light-responsive photoactivities toward photoredox organic transformations including photocatalytic selective reduction of aromatic nitro compounds to amino derivatives and selective oxidation of aromatic alcohols to aldehydes with favorable stability. Moreover, photoredox mechanisms of such alloy NC/TMC photosystems were unveiled. Our work provides an inspiring idea for strategically mediating the charge transfer over atomically precise alloy NCs to advance solar energy conversion.

2. Experimental section

2.1 Preparation

2.1.1 Preparation of CdS nanowires (CdS NWs).[26,27] 1.124 g of cadmium diethyldithiocarbamate [$Cd(S_2CNEt_2)_2$], prepared by precipitation from a stoichiometric mixture of $C_5H_{10}NNaS_2\cdot 3H_2O$ and $CdCl_2\cdot 2.5H_2O$ in DI H_2O, was added into a Teflon-lined stainless-steel autoclave with a capacity of 50 mL. Then, the autoclave was filled with 40 mL of $C_2H_8N_2$ to 80% of the total volume. The autoclave was maintained at 453 K for 24 h and then allowed to cool to room temperature. A yellowish precipitate was collected, washed with absolute ethanol and deionized water (DI H_2O) to remove residual organic solvents. The final products were dried in an oven at 333 K for 12 h.

2.1.2 Preparation of Au_x NCs and bimetallic NCs.[28] A mixture of GSH-protected Au_x NCs and $Au_{1-x}Ag_x$ NCs was synthesized according to previous work with some modifications. Aqueous solutions of $HAuCl_4$ (20 mM, 0.50 mL) and GSH (100 mM, 0.15 mL) were mixed with 4.35 mL of DI H_2O at 25 °C. The reaction mixture was heated to 70 °C under gentle stirring (1200 rpm) for 24 h. The final solution was stored in a refrigerator at 4 °C for further use. The bimetallic $Au_{1-x}Ag_x$ NCs were synthesized under similar conditions, except that a mixture of $HAuCl_4$ (20 mM, 0.50 mL) and $AgNO_3$ (20 mM, 0.10 mL) was used at Ag : Au molar ratios of 0.2 : 1, 0.4 : 1, 0.6 : 1 and 0.8 : 1 for the synthesis. The fabrication of $Au_{1-x}Cu_x$ NCs and $Au_{1-x}Pt_x$ NCs is akin to that of the $Au_{1-x}Ag_x$ NCs by replacing $HAuCl_4$ with $Cu(NO_3)_2$ and chloroplatinic acid hexahydrate ($H_2PtCl_6\cdot 6H_2O$), respectively.

2.1.3 Preparation of MEA-modified TMCs (CdS@MEA). 0.1 g of CdS NWs was first dispersed in DI H_2O (100 mL) by sonication for 10 min, and then 9 mL of 2-mercaptoethylamine (MEA, 0.25 mol L^{-1}) was added into the above mixture under stirring (1000 rpm) and stirred for 1 h under ambient conditions to promote the adsorption of MEA on the CdS NWs. Finally, the MEA-modified CdS NWs (CdS@MEA) were rinsed with ethanol and fully dried in an oven at 333 K.

2.1.4 Preparation of metal NC/TMC heterostructures. 0.1 g of CdS@MEA was dispersed in 20 mL of $Au_{1-x}Ag_x$ NCs solution and stirred (1000 rpm) for 1 h. Then, the mixture was centrifuged, washed with DI H_2O, and dried at 333 K in an oven to obtain the alloy NCs/CdS nanocomposites. For the fabrication of $Au_{1-x}Ag_x$/CdS NW heterostructures, the molar ratio of Ag to Au is controlled to be 0.2 : 1. The detailed procedures for fabricating $Au_{1-x}Ag_x$/CdS NW heterostructures with different loading amounts of $Au_{1-x}Ag_x$ NCs are provided as follows: 0.1 g of CdS@MEA NWs was added into 20 mL of $Au_{1-x}Ag_x$ NC stock solution (0.8 mg mL^{-1}, PH = 2.75) whose concentration is defined as 100%. Then, the stock solution was diluted with DI H_2O according to the volume ratio (*e.g.*, 15% diluted solution consists of 3 mL of the original solution and 17 mL of DI H_2O). The fabrication procedures of $Au_{1-x}Cu_x$/CdS NW and $Au_{1-x}Pt_x$/CdS NW heterostructures are akin to that of $Au_{1-x}Ag_x$/CdS NWs.

2.2 Characterization

Zeta potential (ξ) measurements were carried out on a dynamic light scattering analysis instrument (ZetasizerNano ZS-90). Field-emission scanning electron microscopy (FESEM, Supra55, Carl Zeiss, Germany) was used to characterize the morphologies of the samples. Transmission electron microscopy (TEM), high-resolution (HR) TEM and energy-dispersive spectroscopy (EDS) images were obtained using a JEOL-2010 instrument at an accelerating voltage of 200 kV. The crystal phases of the samples were determined by X-ray diffraction (XRD, X'Pert Pro MPD, Philips, Holland) using Cu Kα radiation at 40 kV and 40 mA. Fourier transform infrared (FTIR) spectra were recorded on a TJ270-30A infrared spectrophotometer. Raman spectra were measured on a Renishaw inVia spectrometer. The optical properties of the samples were probed using a Cary 500 UV-vis diffuse reflectance spectroscopy (DRS) system, with $BaSO_4$ employed as the internal reflectance standard. X-Ray photoelectron spectroscopy (XPS) measurements were performed on an Escalab 250 and the binding energy of the elements was calibrated using the peak at 284.6 eV. The

Brunauer–Emmett–Teller (BET) specific surface area and N_2 adsorption experiments were carried out on an ASAP 2460 instrument. Time-resolved photoluminescence (TRPL) spectra were recorded on a FLS 920 fluorescence lifetime spectrophotometer (Edinburgh, Instruments, UK). The photoluminescence (PL) spectra of the solid samples were measured on a Varian Cary Eclipse spectrophotometer. The concentrations of Au_{1-x}-Ag_x/CdS NWs were quantified by inductively coupled plasma emission spectroscopy (ICP, XSERIES 2 ICP-MS).

2.3 Photocatalytic selective reduction reaction

For the photoreduction reaction, a 300 W Xe lamp (PLS-SXE300D, Beijing Perfect Light co. LTD, China) equipped with a 420 nm cut-off filter ($\lambda > 420$ nm) was used as the irradiation source. 10 mg of catalyst and 40 mg of sodium sulfite (Na_2SO_3) were added into 30 mL of 4-NA aqueous solution (20 mg L^{-1}) in a glass reactor (80 mL). After dark absorption under an inert atmosphere (N_2) for 30 min, the suspension was irradiated with visible light. 3 mL of the solution was withdrawn at different times (0, 30, 60, 90, 120, and 150 s), and then the supernatant was analyzed on a UV-vis spectrophotometer (Thermal Fisher, GENESYS). The procedures for the photoreduction of other aromatic nitro compounds were similar to that of 4-NA. Photoactivities of the samples are defined using the following formulae:

$$\text{Conversion } (\%) = \frac{C_0 - C}{C_0} \times 100\% \quad (1)$$

where C_0 represents the initial concentration of nitroaromatics and C is the concentration after visible light irradiation for a certain time.

2.4 Selective photocatalytic oxidation performances

Selective photocatalytic oxidation of aromatic alcohols to the corresponding aldehydes was carried out as follows: a mixture consisting of 8 mg of catalyst, 0.1 mmol alcohol, and 1.5 mL of benzotrifluoride (BTF) saturated with molecular oxygen was transferred into a 10 mL Pyrex glass bottle. After stirring for 30 min in the dark to obtain an evenly dispersed suspension at adsorption–desorption equilibrium, the glass bottle was then irradiated using a 300 W Xe arc lamp (PLS-SXE300D, Beijing Perfectlight Co. Ltd, China) as the visible light source for a certain time with a UV-CUT filter ($\lambda > 420$ nm). After the reaction, the mixture solution was centrifuged at 12 000 rpm to remove the catalyst and the supernatant was analyzed with a gas chromatograph (SHIMADZU GC-2014C). The conversion of alcohols, yield of aldehydes, and selectivity of the oxidation reaction were calculated using the following formulae:

$$\text{Conversion } (\%) = \frac{C_0 - C_{\text{alcohol}}}{C_0} \times 100\% \quad (2)$$

$$\text{Yield } (\%) = \frac{C_{\text{aldehyde}}}{C_0} \times 100\% \quad (3)$$

$$\text{Selectivity } (\%) = \frac{C_{\text{aldehyde}}}{C_0 - C_{\text{alcohol}}} \times 100\% \quad (4)$$

where c_0 is the initial concentration of alcohols, and c_{alcohol} and c_{aldehyde} are the concentrations of alcohols and aldehydes after the reaction, respectively.

2.5 Photoelectrochemical (PEC) measurements

PEC measurements were carried out on electrochemical workstations (CHI 660E & Gamary Interface 1000 E) in a conventional three-electrode quartz cell using 0.5 M Na_2SO_4 aqueous solution (100 mL, 0.5 M, pH = 6.69) as the electrolyte. A Pt plate was used as the counter electrode, an Ag/AgCl electrode was used as the reference electrode, and the samples coated on fluorine-dope tin oxide (FTO) glass were utilized as the working electrodes. Working electrodes were prepared on FTO glass that was cleaned by sonication in ethanol for 30 min and dried at 353 K. The boundary of FTO glass was protected using scotch tape. The 5 mg sample was dispersed in 0.5 mL of absolute ethyl alcohol by sonication to obtain a slurry which was uniformly spread onto the pretreated FTO glass. After drying in air, the Scotch tape was removed, and the uncoated part of the electrode was isolated with nail polish. The exposed area of the working electrode was 1 cm^2.

3. Results and discussion

Scheme 1 shows the process utilized to fabricate alloy NC ($Au_{1-x}Ag_x$, $Au_{1-x}Pt_x$, $Au_{1-x}Cu_x$)/CdS NW heterostructures. Specifically, the CdS NW substrate is initially modified with MEA molecules, conferring a positively charged surface. Considering that the surface of $Au_{1-x}Ag_x$ NCs (*ca.* 1.7 nm) is capped with GSH ligands possessing various carboxyl (–COO–) functional groups (Fig. S1a and c†), they are negatively charged (Fig. S1d†). Consequently, negatively charged $Au_{1-x}Ag_x$@GSH NCs are electrostatically attracted by the oppositely charged CdS@MEA substrate through electrostatic interaction, thus resulting in the formation of $Au_{1-x}Ag_x$/CdS heterostructures under ambient conditions.

3.1. Characterization of alloy NC/TMC heterostructures

The morphology and microstructure of the samples were probed by Scanning Electron Microscopy (SEM) and Transmission Electron Microscopy (TEM) measurements. As illustrated in Fig. 1a and S4,† pristine CdS NWs exhibit a smooth surface with a typical one-dimensional (1D) morphology with a diameter of 50–70 nm and a length of several micrometers. Fig. 1b and c show the morphologies of CdS@MEA and $Au_{1-x}Ag_x$/CdS NWs, which are similar to those of blank CdS NWs, attributable to the ultrathin MEA coating layer and ultra-small size of $Au_{1-x}Ag_x$ NCs (*ca.* 1.7 nm, Fig. S1b†). As shown in Fig. 1d, the TEM image of the CdS substrate displays a nanowire structure, consistent with the corresponding SEM image. The TEM image of the $Au_{1-x}Ag_x$/CdS NW heterostructure (inset, Fig. 1e) reveals the lattice fringe of 0.245 nm that is attributed to the (102) crystallographic plane of CdS. The HRTEM image of $Au_{1-x}Ag_x$/CdS NWs (Fig. 1f) shows that $Au_{1-x}Ag_x$ NCs are uniformly and intimately distributed on the whole framework of the CdS@MEA NW substrate without aggregation. Note that $Au_{1-x}Ag_x$ NCs do

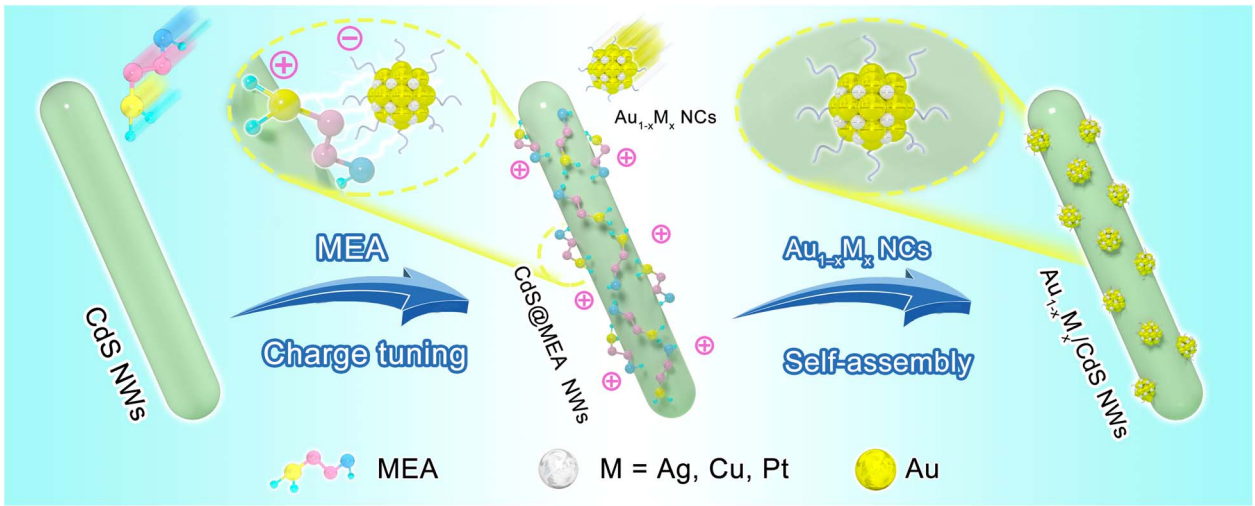

Scheme 1 Schematic illustration for the construction of the $Au_{1-x}Ag_x$/CdS NWs heterostructure.

not exhibit lattice fringes, which is ascribed to their distinct atom-stacking pattern from conventional metal nanocrystals. The element distribution of the $Au_{1-x}Ag_x$/CdS NW heterostructure was investigated using elemental mapping results. Fig. 1g–n display the uniform distribution of Cd, S, Au, Ag, Cl, N, and O elements on the CdS NW substrate, wherein Au, Ag, and O signals originate from the $Au_{1-x}Ag_x$ NCs, the Cl signal originates from the intermediate MEA layer, and Cd & S signals originate from the CdS substrate. The uniform distribution patterns and Energy-Dispersive Spectroscopy (EDS) (Fig. S5†) results confirm the successful deposition of $Au_{1-x}Ag_x$ NCs on the MEA-modified CdS NWs.

X-ray diffraction (XRD) results are probed to determine the crystal structure of the samples. As displayed in Fig. 2a, the peaks at 2θ values of 24.8°, 26.5°, 28.2°, 36.6°, 43.7°, 47.9°, 50.9°, and 51.8° are ascribed to the (100), (002), (101), (102), (110), (103), (200), and (112) crystal planes of greenockite structured CdS (JCPDS No. 41-1049), respectively. However, for the $Au_{1-x}Ag_x$/CdS NW heterostructure, no peaks attributable to $Au_{1-x}Ag_x$ NCs are indiscernible, primarily due to the low deposition amount of $Au_{1-x}Ag_x$ NCs. As displayed in Fig. 2b, Raman spectra of CdS NWs, CdS@MEA NWs and the $Au_{1-x}Ag_x$/CdS NW heterostructure exhibit apparent vibrational peaks at 302 and 605 cm^{-1}, which are assigned to the 1 LO and 2 LO phonon modes of hexagonal CdS,[29,30] respectively. Similarly, no Raman peaks of $Au_{1-x}Ag_x$ NCs are observed, probably due to their amorphous nature. Fourier-Transform Infrared (FTIR) analysis was conducted to further confirm the attachment of $Au_{1-x}Ag_x$ NCs on the CdS NWs. As shown in Fig. 2c and Table S1,† the bands at 2920 and 2851 cm^{-1}, correspond to the $-CH_2$ functional group from the GSH ligands grafted on the $Au_{1-x}Ag_x$ NCs surface. In the FTIR spectra of $Au_{1-x}Ag_x$/CdS NW heterostructures, the band at *ca.* 1635 cm^{-1} exhibits a significantly larger intensity compared with pristine CdS NWs, confirming the successful attachment of $Au_{1-x}Ag_x$ NCs to the CdS NWs substrate.

As shown in Fig. 2d, all the samples exhibit an absorption band edge at approximately 526 nm, which is attributed to the bandgap photoexcitation of the CdS matrix. Notably, light absorption of CdS@MEA is almost identical to that of CdS NWs, suggesting that MEA modification does not alter the optical properties of the CdS substrate. It is worth mentioning that when $Au_{1-x}Ag_x$ NCs are deposited on CdS NWs, light absorption enhancement is observed in the DRS result of the $Au_{1-x}Ag_x$/CdS NW heterostructure, which is attributed to the photosensitization effect of $Au_{1-x}Ag_x$ NCs (Fig. S6†). Furthermore, based on the Kubelka–Munk function *versus* light energy (Fig. 2e), bandgaps of CdS NWs and the $Au_{1-x}Ag_x$/CdS NW heterostructure are estimated to be *ca.* 2.42 eV. Although the bandgap of the $Au_{1-x}Ag$/CdS NW heterostructure does not differ from that of CdS NWs, its enhanced light-harvesting capability within the visible light domain confirms the photosensitization effect of $Au_{1-x}Ag_x$ NCs. As shown in Fig. 2f, the N_2 adsorption–desorption results reveal that both CdS and the $Au_{1-x}Ag_x$/CdS NW heterostructure display type IV isotherms according to the IUPAC classification, indicating that the samples are characteristic of mesoporous materials. As indicated in Table S2,† specific surface areas of CdS and the $Au_{1-x}Ag_x$/CdS NW heterostructure are determined to be 22.276 and 21.713 $m^2\ g^{-1}$, respectively. Compared with CdS NWs, the slight decrease in the specific surface area of $Au_{1-x}Ag_x$/CdS NWs suggests that the decoration of $Au_{1-x}Ag_x$ NCs does not affect the specific surface area of CdS NWs.

As illustrated in Fig. S7a and Table S3,† the survey spectrum of $Au_{1-x}Ag_x$/CdS NWs displays signals for Cd, O, C, S, Au and Ag, which are consistent with the EDS result (Fig. S5†). In the high-resolution Cd 3d spectrum (**Figure 2g(I)**) of CdS NWs, the peaks at 411.68 (Cd $3d_{3/2}$) and 404.94 eV (Cd $3d_{5/2}$) are attributed to the Cd^{2+} species.[31,32] Similarly, in the high-resolution S 2p spectrum (Fig. 2h(I)) of CdS NWs, the peaks at 162.64 (S $2p_{1/2}$) and 161.43 eV (S $2p_{3/2}$) are assigned to the S^{2-} species.[33] The results indicate that the chemical states of Cd and S are not influenced by the deposition of metal NCs. Notably, compared with pristine CdS NWs, the $Au_{1-x}Ag_x$/CdS NW heterostructure exhibits redshifts in the binding energy (BE) for the high-resolution Cd

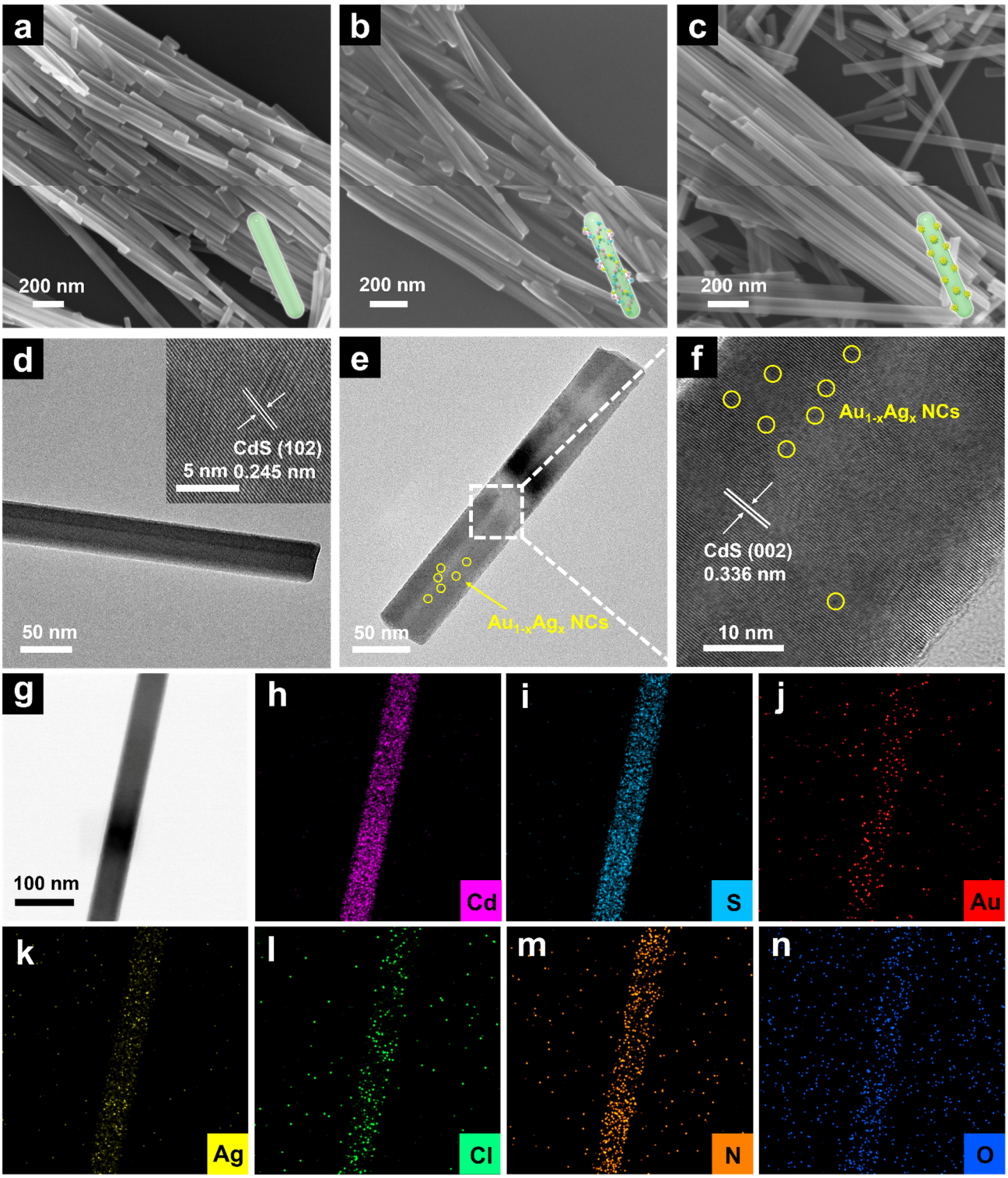

Fig. 1 SEM images of (a) CdS NWs, (b) CdS@MEA NWs, and (c) $Au_{1-x}Ag_x$/CdS NWs heterostructures; (d) TEM and HRTEM (inset) images of CdS NWs; (e) TEM image and (f) HRTEM image of $Au_{1-x}Ag_x$/CdS NWs with (g–n) elemental mapping results.

3d (Fig. 2g(II)) and S 2p (Fig. 2h(II)) spectra albeit they correspond to the same elemental chemical states of Cd^{2+} and S^{2-}, indicating substantial interfacial and electronic interaction between $Au_{1-x}Ag_x$ NCs and the CdS NW substrate. Fig. 2i and j demonstrate the high-resolution Au 4f and Ag 3d spectra of the $Au_{1-x}Ag_x$/CdS NW heterostructure. The Au 4f spectrum (Fig. 2i) reveals two sets of peaks for Au $4f_{5/2}$ and Au $4f_{7/2}$, each of which implies two distinct valence states of Au. Specifically, the peaks at 84.28 and 87.85 eV correspond to Au in the zero-valent state (Au^0), whereas the peaks at 84.77 and 88.45 eV are indicative of

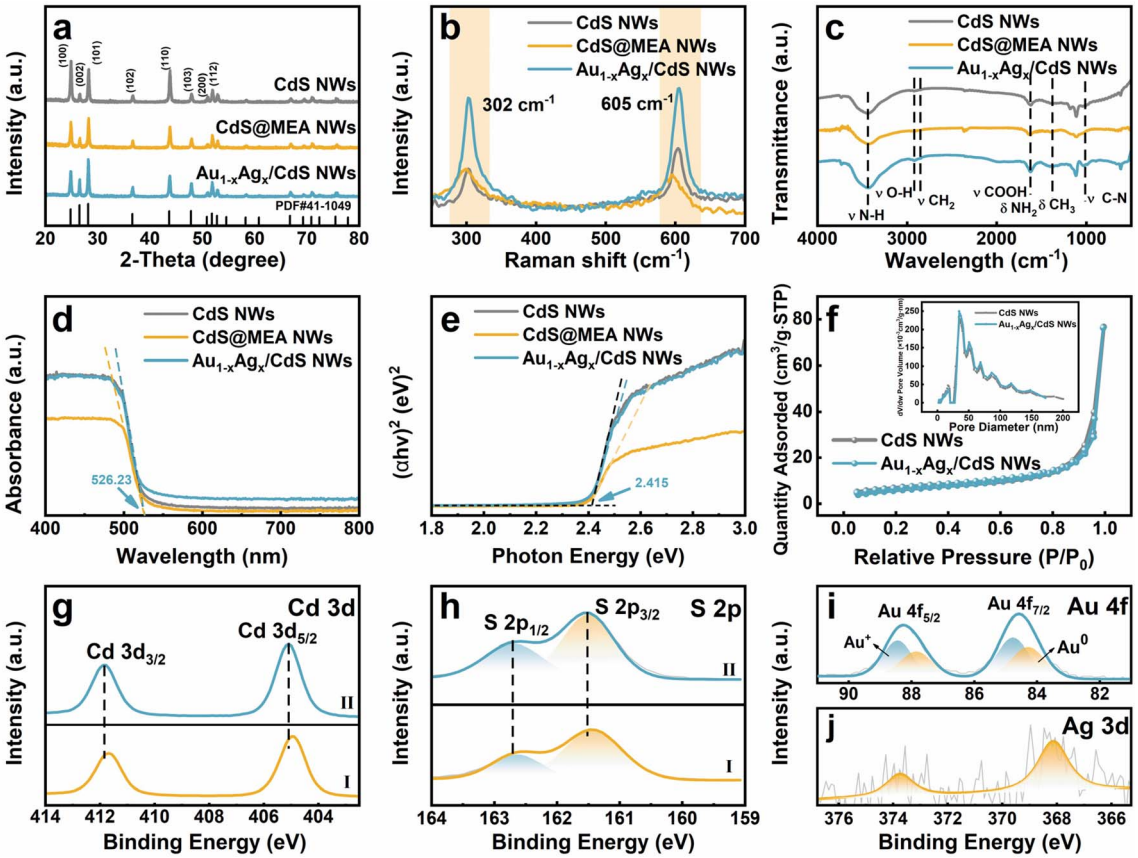

Fig. 2 (a) XRD, (b) Raman, and (c) FTIR results of pristine CdS, CdS@MEA NW and $Au_{1-x}Ag_x$/CdS NW heterostructures; (d) DRS results of pristine CdS, CdS@MEA NW and $Au_{1-x}Ag_x$/CdS NW heterostructures with (e) bandgap determination plots; (f) nitrogen adsorption–desorption isotherms of pristine CdS NWs and $Au_{1-x}Ag_x$/CdS NW heterostructures with pore size distribution patterns in the inset; high-resolution (g) Cd 3d and (h) S 2p spectra of (I) pristine CdS NWs and (II) $Au_{1-x}Ag_x$/CdS NW heterostructures; high-resolution (i) Au 4f and (j) Ag 3d spectra of $Au_{1-x}Ag_x$/CdS NW heterostructures.

Au in the +1 valent state (Au^+).[23,24] As displayed in Fig. 2j, the Ag 3d signal shows two peaks of Ag $3d_{5/2}$ (373.59 eV) and Ag $3d_{3/2}$ (368.35 eV), which are characteristic of Ag^+ species.[34,35] The results confirm the deposition of $Au_{1-x}Ag_x$ NCs on the surface of CdS NWs. To evaluate the generality of our results, we substituted the $Au_{1-x}Ag_x$ NCs in the $Au_{1-x}Ag_x$/CdS NW heterostructures with $Au_{1-x}Cu_x$ NCs and $Au_{1-x}Pt_x$ NCs. The characterization results of $Au_{1-x}Cu_x$/CdS NW and $Au_{1-x}Pt_x$/CdS NW heterostructures including XRD, Raman, DRS and FTIR are provided in Fig. S8 and Table S1.†

3.2 Photocatalytic activities

To explore the photoactivities of the samples, the photocatalytic selective reduction of aromatic nitro compounds to amino derivatives was studied under visible light irradiation ($\lambda > 420$ nm) using ammonium formate as a hole scavenger and N_2 purge. Control experiments were conducted in the absence of the catalyst or under dark conditions, and the results indicate that it is a photocatalytic reaction (Fig. S9†). As shown in Fig. 3a, the loading percentage of $Au_{1-x}Ag_x$ NCs on the CdS NW substrate is controlled by manipulating its concentration during the self-assembly process. The results indicate that photoactivities of $Au_{1-x}Ag_x$/CdS NW heterostructures significantly increase as the concentration of $Au_{1-x}Ag_x$ NCs decreases. Hence, the optimal sample utilized for subsequent analysis was the $Au_{1-x}Ag_x$/CdS NW heterostructure fabricated with $Au_{1-x}Ag_x$ NCs with a volume concentration of 0.05%. Inductively coupled plasma-mass spectrometry (ICP-MS) was employed to quantitatively determine the amount of $Au_{1-x}Ag_x$ NCs in the nanocomposite. According to Table S4,† the loading percentage of $Au_{1-x}Ag_x$ NCs in the $Au_{1-x}Ag_x$/CdS NW heterostructure is approximately 0.0093 wt%. This result is very interesting since such a super-low $Au_{1-x}Ag_x$ NC loading amount unexpectedly leads to a significant photoactivity enhancement, highlighting the remarkable role of alloy NCs as photosensitizers. Fig. 3b presents the comparison of the photocatalytic activities of pristine CdS NWs, CdS@MEA NWs, and $Au_{1-x}Ag_x$/CdS NW heterostructures toward visible-light-responsive photoreduction of 4-nitroaniline (4-NA). Notably, the $Au_{1-x}Ag_x$/CdS NW heterostructure exhibits optimal photoactivity compared with CdS NW and CdS@MEA NW counterparts, signifying the cooperative synergy between CdS NWs and $Au_{1-x}Ag_x$ NCs during the photocatalytic reaction. It is noteworthy that the enhanced photoactivity of CdS@MEA NW compared with CdS NWs signifies the pivotal role of MEA as an interfacial electron

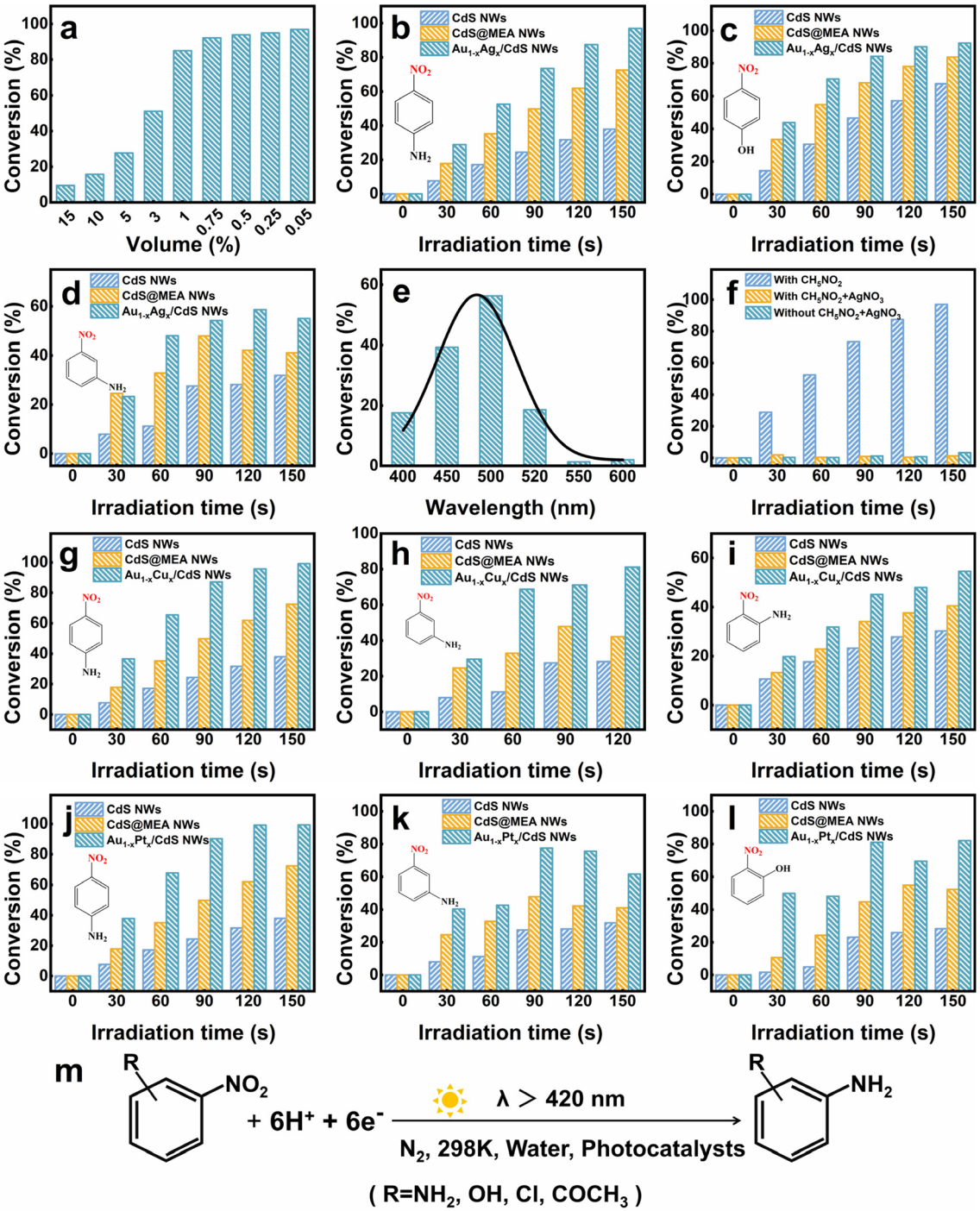

Fig. 3 (a) Photoactivities of $Au_{1-x}Ag_x$/CdS NW heterostructures with different loading amounts of $Au_{1-x}Ag_x$ NCs. Photoactivities of pristine CdS NWs, CdS@MEA NWs, and $Au_{1-x}Ag_x$/CdS NW heterostructures toward the selective photoreduction of nitroaromatics, including (b) 4-NA, (c) 4-NP, and (d) 3-NA under visible light irradiation ($\lambda > 420$ nm) upon adding ammonium formate as a hole quencher. (e) Action spectrum of the $Au_{1-x}Ag_x$/CdS NW heterostructure for photocatalytic 4-NA reduction; (f) photoreduction of 4-NA over the $Au_{1-x}Ag_x$/CdS NW heterostructure with the addition of ammonium formate and ammonium formate + $AgNO_3$ or without the addition of ammonium formate + $AgNO_3$ in the reaction system. Photoactivities of pristine CdS NWs, CdS@MEA NWs, and $Au_{1-x}Cu_x$/CdS NW heterostructures toward the selective photoreduction of nitroaromatics, including (g) 4-NA, (h) 3-NA, and (i) 2-NA under visible light irradiation ($\lambda > 420$ nm); photoactivities of pristine CdS NWs, CdS@MEA NWs, and $Au_{1-x}Pt_x$/CdS NW heterostructures toward the selective photoreduction of nitroaromatics, including (j) 4-NA, (k) 3-NA, and (l) 2-NP along with (m) reaction model under the current experimental conditions.

transport mediator, thereby enhancing the charge separation and enhancing the photoactivities. In addition, as shown in Fig. S10,† MEA exhibits no absorption in the visible domain, ruling out the possibility of optical change for the alloy NCs/TMC heterostructure due to the attachment of MEA at the interfacial domain. In other studies, MEA did not function as

a photosensitizer in the current photosystem. Additionally, as shown in Fig. 3c and d, similar photoactivity improvements are observed in the photoreduction of other nitroaromatic compounds, such as 4-nitrophenol (4-NP) and 3-nitroaniline (3-NA); significantly, the $Au_{1-x}Ag_x$/CdS NW heterostructure consistently outperforms pristine CdS NWs and CdS@MEA NWs in photoactivity. This confirms the critical contribution of $Au_{1-x}Ag_x$ NCs to the improved photocatalytic performances of the $Au_{1-x}Ag_x$/CdS NW heterostructure.

Considering that stability is a primary concern when employing alloy NCs for photocatalytic applications, the robustness of the catalysts was assessed through cyclic reactions. As indicated by Fig. S11,† the photocatalytic activity of the $Au_{1-x}Ag_x$/CdS NW heterostructure demonstrates modest stability. The action spectrum of the $Au_{1-x}Ag_x$/CdS NW heterostructure was explored. As illustrated in Fig. 3e, an apparent peak is observed within the wavelength profile of 400–520 nm, confirming the significant role of the photoexcitation of the CdS NWs matrix. Fig. 3f presents the photocatalytic activities of the $Au_{1-x}Ag_x$/CdS NW heterostructure with and without adding an electron scavenger ($AgNO_3$). The results indicate that the photoactivity of $Au_{1-x}Ag_x$/CdS NWs is entirely extinguished upon adding the electron scavenger ($AgNO_3$), affirming the significance of electrons in triggering the photoreduction catalysis. Note that the photoactivity of the $Au_{1-x}Ag_x$/CdS NW heterostructure was markedly diminished without the incorporation of a hole scavenger (ammonium formate), highlighting the importance of quenching holes in the photoreduction reaction.

To verify the universal photosensitization effect of metal NCs, photoactivities of alloy NCs [$Au_{1-x}Cu_x$ and $Au_{1-x}Pt_x$]/CdS heterostructures toward the photoreduction of nitroaromatic compounds were also investigated under the identical experimental conditions. As shown in Fig. 3g, photoactivity of the optimal $Au_{1-x}Cu_x$/CdS NWs is approximately 2 times larger than that of pristine CdS NWs. Moreover, as displayed in Fig. 3h, i and S12a–c,† besides 4-NA, similar results are observed in the selective photoreduction of other aromatic nitro compounds over the $Au_{1-x}Cu_x$/CdS NW heterostructure, including 3-nitroaniline (3-NA), 2-nitroaniline (2-NA), nitrobenzene (NB), 4-nitrotoluene (4-NT), and 1-bromo-4-nitrobenzene. Alternatively, as displayed in Fig. 3j–l, S12d and e,† analogous results are observed in the selective photoreduction of aromatic nitro compounds over the $Au_{1-x}Pt_x$/CdS NW heterostructure including 4-nitroaniline (4-NA), 3-nitroaniline (3-NA), 2-nitrophenol (2-NP), 1-chloro-4-nitrobenzene, and nitrobenzene (NB). Thus, the results concurrently reveal the general roles of $Au_{1-x}Cu_x$ NCs and $Au_{1-x}Pt_x$ NCs in enhancing the photoactivities of $Au_{1-x}Cu_x$/CdS NW and $Au_{1-x}Cu_x$/CdS NW heterostructures.

Photocatalytic selective oxidation of aromatic alcohols to the corresponding aldehydes over $Au_{1-x}Ag_x$/CdS NW heterostructures was probed. As shown in Fig. 4a, with regard to the photocatalytic selective oxidation of benzyl alcohol (BA), the conversion and yield of CdS NWs, CdS@MEA NWs and $Au_{1-x}Ag_x$/CdS NW heterostructures reach 18.12%, 8.94%, and 52.87%, respectively, coupled with 100% selectivity under visible light exposure. Notably, the $Au_{1-x}Ag_x$/CdS NW heterostructure demonstrates superior photoactivity over other counterparts. Additionally, the photocatalytic selective oxidation of a variety of aromatic benzylic alcohols including benzyl alcohol (BA), *p*-methylbenzyl alcohol (MBA), and *p*-chlorobenzyl alcohol (CBA), bearing substituents from electron-donating groups to electron-withdrawing groups, over these three samples was further explored. Fig. 4b and c suggest that the $Au_{1-x}Ag_x$/CdS NW heterostructure consistently exhibits significantly higher conversion and yield than those of pristine CdS NW and CdS@MEA NW counterparts in the photocatalytic selective oxidation of *p*-methylbenzyl alcohol and *p*-chlorobenzyl alcohol. The results indicate the general photosensitization effect of the $Au_{1-x}Ag_x$/CdS NW heterostructure in facilitating the selective organic transformations when subjected to visible light irradiation.

Fig. 4d demonstrates the photoactivities of $Au_{1-x}Ag_x$/CdS NWs with the addition of different scavengers, enabling the identification of the predominant reactive species during the photocatalytic reaction. To this end, benzoquinone (BQ), potassium persulfate ($K_2S_2O_8$), ammonium oxalate (AO), and *tert*-butyl alcohol (*t*-BuOH) were added into the reaction system for trapping superoxide radicals ($^{\bullet}O_2^-$), electrons (e^-), holes (h^+), and hydroxyl radicals ($^{\bullet}OH$), respectively. Specifically, when $K_2S_2O_8$ was added into the reaction system for trapping electrons, the high photoactivity of the $Au_{1-x}Ag_x$/CdS NW heterostructure is not altered, confirming the negligible role of electrons in the photocatalytic selective oxidation of BA. When BQ and *t*-BuOH were added into the reaction system as the superoxide radical ($^{\bullet}O_2^-$) and hydroxyl radical ($^{\bullet}OH$) scavengers, the photoactivities of the $Au_{1-x}Ag_x$/CdS NW heterostructure were considerably decreased, confirming that superoxide radicals ($^{\bullet}O_2^-$) and hydroxyl radicals ($^{\bullet}OH$) exert substantial influence on improving the photoactivities of the $Au_{1-x}Ag_x$/CdS NW heterostructure. When AO was added into the reaction system for quenching holes, the photoactivity of the $Au_{1-x}Ag_x$/CdS NW heterostructure was substantially reduced, indicating that the photocatalytic selective oxidation of BA over the $Au_{1-x}Ag_x$/CdS NW heterostructure is primarily driven by holes. The general contributing roles of the active species follow the order of $h^+ > {}^{\bullet}O_2^- > {}^{\bullet}OH > e^-$. Alternatively, a control experiment with a N_2 purge was carried out to evaluate the importance of dissolved O_2 in enhancing the photoactivity of the $Au_{1-x}Ag_x$/CdS NW heterostructure. As displayed in Fig. 4d, the photoactivity of the $Au_{1-x}Ag_x$/CdS NW heterostructure using N_2 saturated BTF solvent is markedly lower than that using O_2-saturated BTF, indicating that dissolved O_2 plays an important role in improving the photoactivity of the $Au_{1-x}Ag_x$/CdS NW heterostructure. This is understandable since dissolved O_2 is indispensable for the generation of oxygen-containing active species which synergistically contribute to the enhanced photoactivity. The correlation of these active species can be reflected by the formulae below:[36]

$$O_2 + e^- \rightarrow {}^{\bullet}O_2^- \quad (5)$$

$$2{}^{\bullet}O_2^- + 2H^+ \rightarrow H_2O_2 + O_2 \quad (6)$$

$$H_2O_2 + {}^{\bullet}O_2^- \rightarrow {}^{\bullet}OH + OH^- + O_2 \quad (7)$$

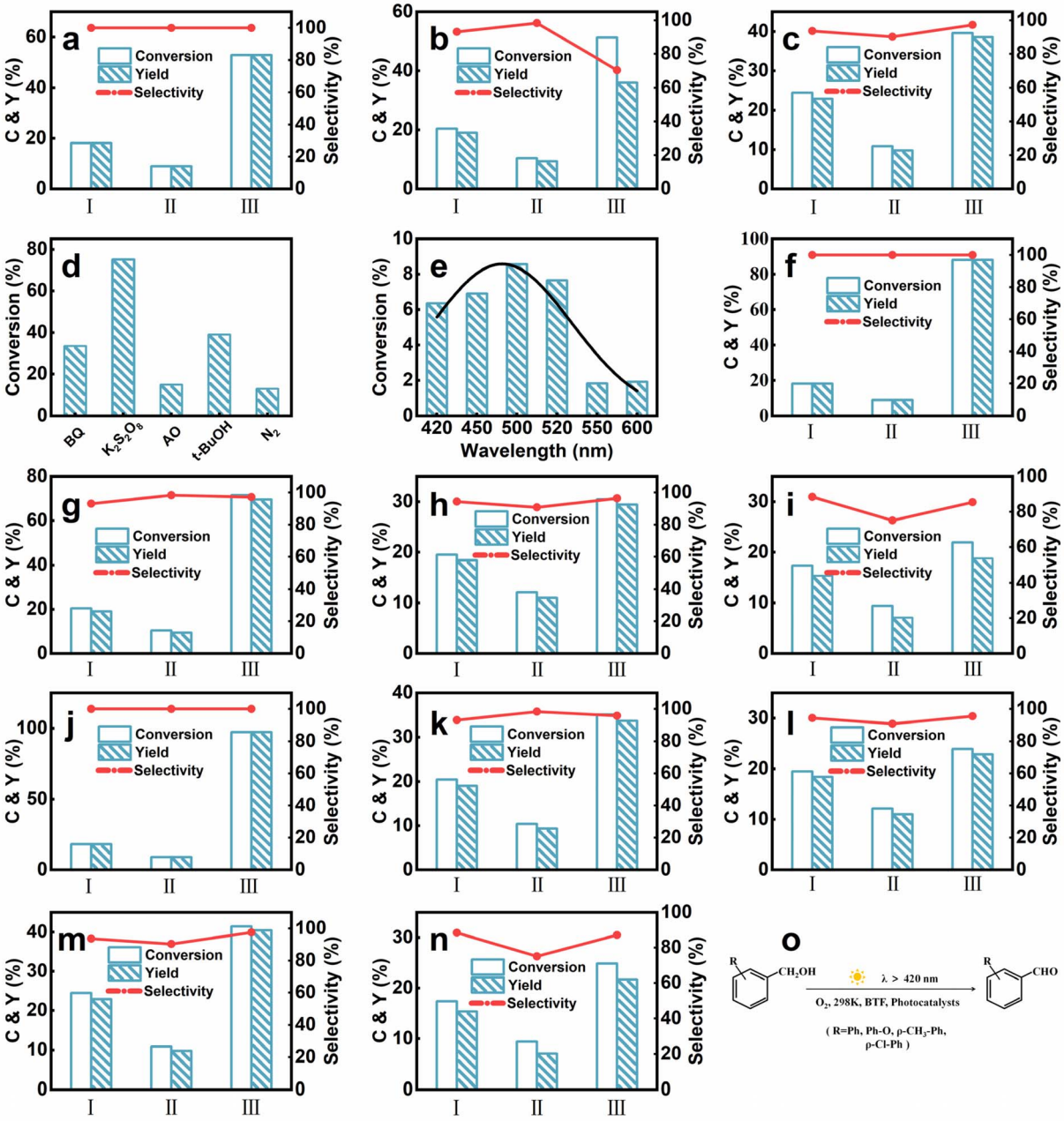

Fig. 4 Photoactivities of (I) pristine CdS NWs, (II) CdS@MEA NWs and (III) $Au_{1-x}Ag_x$/CdS NW heterostructures toward the photocatalytic selective oxidation of aromatic alcohols, including (a) benzyl alcohol, (b) *p*-methylbenzyl alcohol, and (c) *p*-chlorobenzyl alcohol, to the corresponding aldehydes under visible light irradiation (λ > 420 nm) for 4 h; (d) photocatalytic selective oxidation of BA over the $Au_{1-x}Ag_x$/CdS NW heterostructure for 4 h by adding BQ, $K_2S_2O_8$, AO, *t*-BuOH and N_2 as scavengers for quenching superoxide radicals ($^{\bullet}O_2^-$), electrons (e^-), holes (h^+) and hydroxyl radicals ($^{\bullet}OH$), respectively, and (e) photocatalytic oxidation of BA over the $Au_{1-x}Ag_x$/CdS NW heterostructure under monochromatic light irradiation. Photoactivities of (I) pristine CdS NWs, (II) CdS@MEA NWs and (III) $Au_{1-x}Cu_x$/CdS NW heterostructures toward the selective oxidation of aromatic alcohols, including (f) BA, (g) *p*-methylbenzyl alcohol, (h) *p*-fluorobenzyl alcohol and (i) *p*-nitrobenzyl alcohol, under visible light irradiation (λ > 420 nm) for 4 h. Photoactivities of (I) pristine CdS NWs, (II) CdS@MEA NWs and (III) $Au_{1-x}Pt_x$/CdS NW heterostructures toward the selective oxidation of aromatic alcohols, including (j) BA, (k) *p*-methylbenzyl alcohol, (l) *p*-fluorobenzyl alcohol, (m) *p*-chlorobenzyl alcohol, and (n) *p*-nitrobenzyl alcohol under visible light irradiation (λ > 420 nm) for 4 h; (o) photocatalytic selective oxidation reaction model under the current experimental conditions.

As displayed in Fig. 4e, a substantial peak extending from 420 to 600 nm is observed in the action spectrum of the $Au_{1-x}Ag_x$/CdS NW heterostructure toward the photocatalytic selective oxidation of BA, confirming that the excellent photoactivities of the $Au_{1-x}Ag_x$/CdS NW heterostructure stem from the band-gap-photoexcitation of CdS NWs. A similar strategy was employed to fabricate a series of other alloy NCs [$Au_{1-x}Cu_x$, $Au_{1-x}Pt_x$]/CdS NW heterostructures for

photocatalytic selective oxidation of aromatic alcohols to aldehydes under visible light irradiation. As reflected by Fig. 4f–i, the $Au_{1-x}Cu_x$/CdS NW heterostructure still exhibits optimal photoactivities toward the selective oxidation of benzyl alcohol, *p*-methylbenzyl alcohol, *p*-fluorobenzyl alcohol and *p*-nitrobenzyl alcohol to the corresponding aldehydes with high conversion and selectivity under visible light, which are superior to those of pristine CdS NW and CdS@MEA NW counterparts. As reflected in Fig. 4j–n, the $Au_{1-x}Pt_x$/CdS NW heterostructure always shows significantly improved photoactivities in comparison with pristine CdS NW and CdS@MEA NW counterparts, strongly reflecting the highly efficient and multifarious photoactivities of the $Au_{1-x}Pt_x$/CdS NW heterostructure. The results confirm the general roles of $Au_{1-x}Ag_x$, $Au_{1-x}Cu_x$ and $Au_{1-x}Pt_x$ NCs as photosensitizers in accelerating the photocatalytic selective organic transformation of heterostructures.

Photoelectrochemical (PEC) measurements were performed to evaluate the interfacial charge separation efficiency of the samples. As depicted in Fig. 5a, the $Au_{1-x}Ag_x$/CdS NW heterostructure exhibits a considerably enhanced photocurrent compared with pristine CdS NWs under visible light irradiation, corroborating that the integration of $Au_{1-x}Ag_x$ NCs with CdS NWs effectively mitigates charge recombination. Electrochemical impedance spectroscopy (EIS) results, as shown in Fig. 5b, reveal that the $Au_{1-x}Ag_x$/CdS NW heterostructure exhibits a smaller semicircle arc radius under visible light irradiation relative to CdS NWs, indicative of its lower interfacial charge transfer resistance (Table S5†) and thus a more efficient charge separation efficiency. The results confirm that the heterostructure engendered by integrating $Au_{1-x}Ag_x$ NCs with CdS NWs enhances the separation and transfer of photogenerated electron–hole pairs. Furthermore, the open-circuit voltage decay (OCVD) results (Fig. 5c) suggest that the $Au_{1-x}Ag_x$/CdS NW heterostructure possesses a larger photovoltage and a more prolonged electron lifespan (Fig. 5d) compared with blank CdS NWs. This once again verifies that charge separation is enhanced over the $Au_{1-x}Ag_x$/CdS NW heterostructure. As shown in Fig. S13†, the PEC performances of $Au_{1-x}Cu_x$/CdS NW and $Au_{1-x}Pt_x$/CdS NW heterostructures also demonstrate improved charge separation efficiency, prolonged electron lifetime, and smaller interfacial charge transfer resistance relative to blank CdS NWs, verifying the general role of $Au_{1-x}Cu_x$ and $Au_{1-x}Pt_x$ NCs as photosensitizers.

Photoluminescence (PL) spectroscopy is considered as an efficient tool to assess the carrier separation efficiency of a photocatalyst. The emission observed in the PL results is caused by the recombination of photo-excited electron–hole pairs, and the decreased PL intensity reflects an increase in charge recombination. As shown in Fig. 5e, the $Au_{1-x}Ag_x$/CdS NW heterostructure exhibits lower PL intensity compared with CdS NWs, suggesting that charge recombination over the $Au_{1-x}Ag_x$/CdS NW heterostructure is significantly suppressed. As displayed in Fig. 5f, time-resolved PL measurements were performed to further probe the charge transfer kinetics of the $Au_{1-x}Ag_x$/CdS NW heterostructure, and the results are summarized in Table S6.† Specifically, when $Au_{1-x}Ag_x$ NCs are loaded on the surface of CdS NWs, there is an increase in the PL lifetime of the CdS NW substrate due to hole transfer. Based on the PL results, we infer that, in addition to the injection of electrons from the LUMO level of $Au_{1-x}Ag_x$ NCs to the conduction band (CB) of CdS, holes from the valence band (VB) of CdS are also transferred to the HOMO level of $Au_{1-x}Ag_x$ NCs to promote charge separation, following a type-II charge transfer pathway.[37,38] This charge transport characteristic increases the electron lifetime, thereby enhancing the carrier separation efficiency.[39]

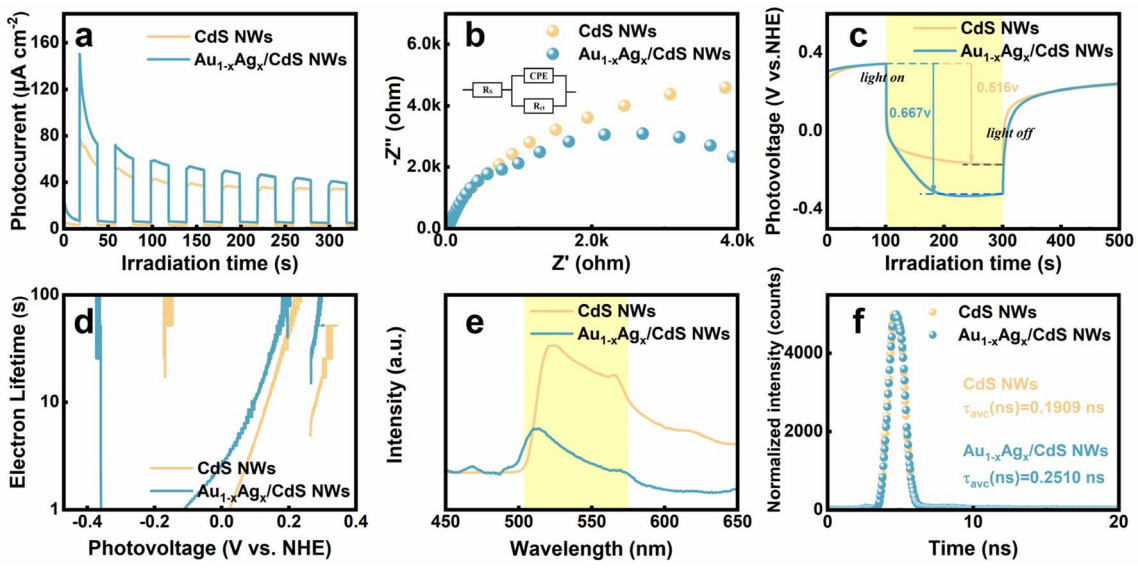

Fig. 5 (a) On–off transient photocurrents, (b) EIS results, (c) open-circuit potential decay plots, (d) electron lifetime (τ_n), and (e) PL spectra of pristine CdS NWs and the $Au_{1-x}Ag_x$/CdS NW heterostructure with an excitation wavelength of 350 nm, along with (f) time-resolved transient PL decay spectra for pristine CdS NWs and the $Au_{1-x}Ag_x$/CdS NW heterostructure.

3.3. Photocatalytic mechanism

The energy level positions of the CdS NW substrate are determined by Mott–Schottky (M–S) and DRS analyses. As shown in Fig. S14,† the M–S results indicate that the flat band potential of CdS NWs is −0.450 V relative to the normal hydrogen electrode (NHE). Based on the bandgap (E_g) value of 2.42 eV determined by the DRS results (Fig. 2e), the VB position of CdS is determined to be 1.97 V *vs.* NHE by applying the equation E_g = VB − CB. Furthermore, according to the UV-vis absorption spectra (Fig. S1e†) and cyclic voltammetry (CV) results (Fig. S15a†), the LUMO and HOMO levels of $Au_{1-x}Ag_x$ NC are determined to be approximately −2.24 V and 0.66 V *vs.* NHE (Fig. 6c and S15b†), respectively. The HOMO and LUMO levels of $Au_{1-x}Cu_x$ NCs and $Au_{1-x}Pt_x$ NCs were also determined by analogous methods (Fig. 6d, e, S15d and f†).

It is well-established that *in situ* XPS represents an effective technique to analyze the surface chemistry and charge transport mechanism of photocatalysts.[40] A higher shift in the binding energies of core elements indicates a reduction in electron density and *vice versa*.[41] As shown in Fig. 6a and b, under visible light irradiation, the binding energies of Au 4f and Ag 3d elements in the $Au_{1-x}Ag_x$/CdS NW heterostructure are significantly red-shifted compared with those in the dark, indicating that photoelectrons are transferred from $Au_{1-x}Ag_x$ NCs to CdS

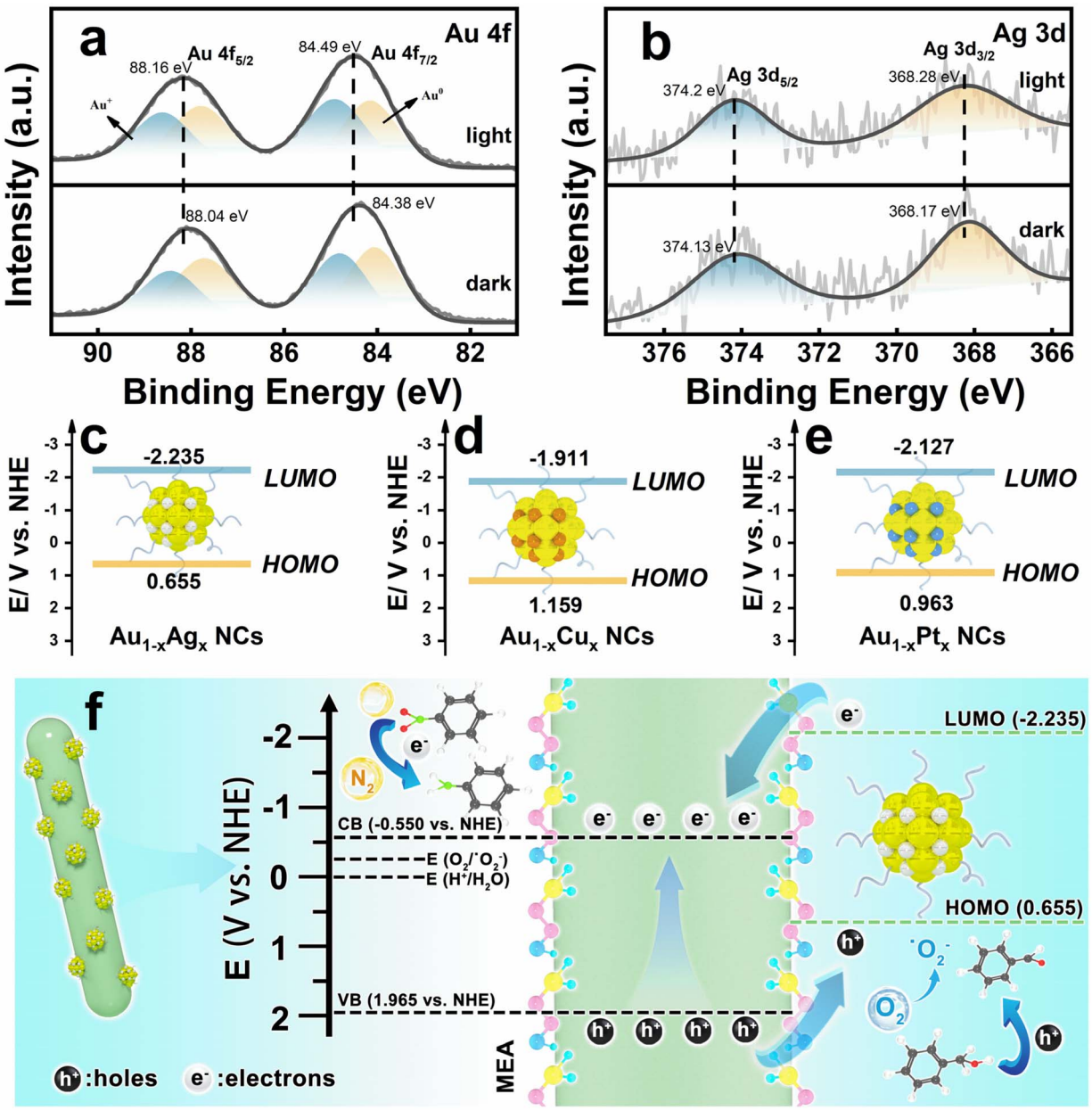

Fig. 6 *In situ* high-resolution XPS spectra of (a) Au 4f and (b) Ag 3d for the $Au_{1-x}Ag_x$/CdS NWs heterostructure; schematic illustration of the energy level alignment of (c) $Au_{1-x}Ag_x$ NCs, (d) $Au_{1-x}Cu_x$ NCs, and (e) $Au_{1-x}Pt_x$ NCs; (f) schematic diagram depicting the photocatalytic mechanism of the $Au_{1-x}Ag_x$/CdS NW heterostructure.

under light irradiation. This provides crucial evidence for determining the interfacial charge transfer pathway over the $Au_{1-x}Ag_x$/CdS NW heterostructure under visible light irradiation. Similarly, as depicted in Fig. S16c and d,† under visible light irradiation, the binding energies of N 1s and Cl 2p for the $Au_{1-x}Ag_x$/CdS NW heterostructure shift to higher values, indicating a decreased electron density on the MEA. Evidently, under visible light irradiation, photoelectrons migrate from $Au_{1-x}Ag_x$ NCs through the intermediate MEA layer to the CdS substrate. Clearly, the MEA intermediate layer acts as a charge mediator to expedite the directional flow of electrons from alloy NCs to TMCs, thereby enhancing the charge separation and improving the photocatalytic activities.

Based on the above analysis, the photocatalytic mechanism of the alloy NCs [$Au_{1-x}Ag_x$, $Au_{1-x}Pt_x$, and $Au_{1-x}Cu_x$]/CdS NW heterostructures is proposed. As illustrated in Fig. 6f, under visible light irradiation, alloy NC [$Au_{1-x}Ag_x$, $Au_{1-x}Pt_x$, and $Au_{1-x}Cu_x$] ingredients of the heterostructure are photoexcited, generating electron–hole pairs in the LUMO and HOMO energy levels, respectively. Given that the LUMO levels of these alloy NCs are more negative than the CB of CdS, and their HOMO levels are lower than the VB of CdS (1.965 V *vs.* NHE), type II energy level alignment is thus established. Consequently, electrons from the LUMO of alloy NCs are more readily transferred to the CB of CdS, while holes migrate from the VB of CdS to the HOMO level of alloy NCs. It is worth noting that the ultrathin MEA intermediate layer serves as an electron relay mediator to increase the directional electron flow from alloy NCs to the CdS substrate. Regarding the photocatalytic selective reduction of aromatic nitro compounds (Fig. S17†), electrons flowing to the CB of CdS are the sole active species capable of photoreducing aromatic nitro compounds to amino derivatives, while the holes transferring to the HOMO level of alloy NCs are completely quenched by a scavenger (ammonium formate),[42] thus fulfilling the photoreduction catalysis. For the photocatalytic selective oxidation of aromatic alcohols to the corresponding aldehydes (Fig. S18†), $^{\bullet}O_2^-$ and h^+ are identified as the primary active species, both of which are responsible for the oxidation reaction. More specifically, electrons injected into the CB of CdS are captured to generate Cd^{III} species and the alcohol molecules are adsorbed on the CdS surface to form structure **II** through deprotonation.[43,44] Subsequently, the adsorbent alcohol molecule first reacts with holes and then deprotonates to form carbon radicals, while electrons are captured by Cd^{III} to form Cd^{IV}. It is worth noting that electrons can directly combine with the dissolved O_2 molecules to engender superoxide ($^{\bullet}O_2^-$) radicals [$E^{\circ}(O_2/^{\bullet}O_2^-) = -0.284$ V *vs.* NHE].[45] In this regard, the thus-formed $^{\bullet}O_2^-$ radicals take part in the oxidation of aromatic alcohols to aldehydes and attack the carbon radical to form intermediate **IV**, for which the interactions between the C–O bonds of the alcohol and O–O bonds of dioxygen may be synergistically realized through the oxygen-bridged structure **IV**.[46] Alternatively, holes in the HOMO of alloyed NCs can also directly oxidize the aromatic alcohols to aldehydes considering their high oxidation capability, fulfilling the selective photocatalytic oxidation process.

4. Conclusions

In summary, tailor-made alloy NCs [$Au_{1-x}Ag_x$, $Au_{1-x}Pt_x$, and $Au_{1-x}Cu_x$] are precisely anchored on the CdS NWs by a simple, efficient, and universal electrostatic self-assembly strategy combined with favorable interface configuration modulation. The self-assembled alloy NC/CdS heterostructures exhibit significantly enhanced photocatalytic activities for multifarious visible-light-responsive photoredox catalysis reactions, including the photocatalytic selective reduction of aromatic nitro compounds to amino derivatives and the selective oxidation of aromatic alcohols to aldehydes, due to the construction of favorable type II energy level alignment between alloy NCs and CdS. The unidirectional transfer of electrons from alloy NCs to CdS significantly improves the charge separation efficiency, enhancing the photocatalytic activities. Our work provides a novel approach to achieve fine tuning of spatially vectorial charge motion through simple yet judicious interface modulation for solar energy conversion into chemical energy.

Data availability

The data supporting this article have been included as part of the ESI.†

Conflicts of interest

There are no conflicts to declare.

Acknowledgements

The support provided by the award Program for Minjiang scholar professorship is greatly acknowledged. This work was financially supported by the National Natural Science Foundation of China (No. 21703038 and 22072025). Financial support from the State Key Laboratory of Structural Chemistry, Fujian Institute of Research on the Structure of Matter, Chinese Academy of Sciences is acknowledged (No. 20240018).

References

1 X. S. Du and R. C. Jin, *ACS Nano*, 2019, **13**, 7383.
2 Z. T. Luo, X. Yuan, Y. Yu, Q. B. Zhang, D. T. Leong, J. Y. Lee and J. P. Xie, *J. Am. Chem. Soc.*, 2012, **134**, 16662.
3 Y. S. Chen and P. V. Kamat, *J. Am. Chem. Soc.*, 2014, **136**, 6075.
4 F. X. Xiao, Z. Zeng and B. Liu, *J. Am. Chem. Soc.*, 2015, **137**, 10735.
5 Q. Q. Shi, Z. X. Qin, S. Sharma and G. Li, *Chem. Rec.*, 2021, **21**, 879.
6 Z. Zeng, Y. B. Li, S. F. Chen, P. Chen and F.-X. Xiao, *J. Mater. Chem. A*, 2018, **6**, 11154.
7 R. Khan, M. H. Naveen, M. A. Abbas, J. Lee, H. Kim and J. H. Bang, *ACS Energy Lett.*, 2020, **6**, 24.
8 Y. X. Du, H. T. Sheng, D. Astruc and M. Z. Zhu, *Chem. Rev.*, 2019, **120**, 526.

9 Y. Wei, Y. Z. Wu, J. Wang, Y. H. Wu, Z. L. Weng, W. Y. Huang, K. Yang, J. L. Zhang, Q. Li, K. Q. Lu and B. Han, *J. Mater. Chem. A*, 2024, **12**, 18986.
10 T. Kawawaki, Y. Negishi and H. Kawasaki, *Nanoscale Adv.*, 2020, **2**, 17.
11 F. X. Xiao, S. F. Hung, J. Miao, H. Y. Wang, H. Yang and B. Liu, *Small*, 2014, **11**, 554.
12 X. C. Dai, M. H. Huang, Y. B. Li, T. Li, S. Hou, Z. Q. Wei and F.-X. Xiao, *J. Phys. Chem. C*, 2020, **124**, 4989.
13 Q. L. Mo, B. J. Liu and F.-X. Xiao, *J. Phys. Chem. C*, 2021, **125**, 22421.
14 T. Liu, L. Miao, F. Y. Yao, W. X. Zhang, W. X. Zhao, D. S. Yang, Q. Feng and D. W. Hu, *Inorg. Chem.*, 2024, **63**, 1.
15 Y. H. Wu, Y. Q. Yan, Y. Wei, J. Wang, A. Li, W. Y. Huang, J. L. Zhang, K. Yang and K. Q. Lu, *Int. J. Hydrogen Energy*, 2024, **78**, 452.
16 I. Chakraborty and T. Pradeep, *Chem. Rev.*, 2017, **117**, 8208.
17 S. Hou, M. H. Huang and F. X. Xiao, *J. Mater. Chem. A*, 2022, **10**, 7006.
18 R. C. Jin, C. J. Zeng, M. Zhou and Y. X. Chen, *Chem. Rev.*, 2016, **116**, 10346.
19 Y. B. Li and F. X. Xiao, *J. Mater. Chem. A*, 2023, **11**, 589.
20 Z. Q. Wei, S. Hou, X. Lin, S. Xu, X. C. Dai, Y. H. Li, J. Y. Li, F. X. Xiao and Y.-J. Xu, *J. Am. Chem. Soc.*, 2020, **142**, 21899.
21 X. Yan, X. Y. Fu and F. X. Xiao, *Adv. Funct. Mater.*, 2023, **33**, 2303737.
22 B. Tang, S. C. Zhu, H. Liang, S. Li, B. J. Liu and F.-X. Xiao, *J. Mater. Chem. A*, 2022, **10**, 4032.
23 Z. Y. Li, Y. H. Chen, J. R. Zhu, Q. Chen, S. J. Lu and F.-X. Xiao, *Inorg. Chem.*, 2023, **62**, 16965.
24 P. Su, B. Tang and F. X. Xiao, *Small*, 2023, **20**, 2307619.
25 G. Wu, Q. L. Mo, Y. Xiao, K. Wang, X. Z. Ge, S. R. Xu, J. L. Li, Y. Q. Shao and F. X. Xiao, *Inorg. Chem.*, 2022, **62**, 520.
26 Q. L. Nie, Q. L. Yuan, Q. S. Wang and Z. J. Xu, *Mater. Sci.*, 2004, **39**, 5611.
27 S. Q. Liu and Y.-J. Xu, *Nanoscale*, 2013, **5**, 9330.
28 D. Hikosou, S. Saita, S. Miyata, H. Miyaji, T. Furuike, H. Tamura and H. Kawasaki, *J. Phys. Chem. C*, 2018, **122**, 12494.
29 M. Abdulkhadar and B. Thomas, *Nanostruct. Mater.*, 1995, **5**, 289.
30 J. Lee, *Thin Solid Films*, 2004, **451–452**, 170.
31 V. L. Colvin, A. N. Goldstein and A. P. Alivisatos, *J. Am. Chem. Soc.*, 1992, **114**, 5221.
32 S. Rengaraj, S. Venkataraj, S. H. Jee, Y. Kim, C. w. Tai, E. Repo, A. Koistinen, A. Ferancova and M. Sillanpää, *Langmuir*, 2010, **27**, 352.
33 K. Ojha, T. Debnath, P. Maity, M. Makkar, S. Nejati, K. V. Ramanujachary, P. K. Chowdhury, H. N. Ghosh and A. K. Ganguli, *J. Phys. Chem. C*, 2017, **121**, 6581.
34 H. Yao, R. Kobayashi and Y. Nonoguchi, *J. Phys. Chem. C*, 2016, **120**, 128.
35 K. Y. Zheng, X. Yuan, K. Kuah, Z. T. Luo, Q. F. Yao, Q. B. Zhang and J. P. Xie, *Chem. Commun.*, 2015, **51**, 15165.
36 S. Xu, M. H. Huang, T. Li, Z. Q. Wei, X. Lin, X. C. Dai, S. Hou, X. Y. Fu and F. X. Xiao, *J. Mater. Chem. A*, 2020, **8**, 8360.
37 S. Khanchandani, S. Kundu, A. Patra and A. K. Ganguli, *J. Phys. Chem. C*, 2012, **116**, 23653.
38 Z. F. Shao, Y. Wang, Y. F. Zhang, G. Zhu, X. J. Yang and M. Zhong, *J. Photochem. Photobiol., A*, 2018, **364**, 657.
39 S. A. Ivanov, A. Piryatinski, J. Nanda, S. Tretiak, K. R. Zavadil, W. O. Wallace, D. Werder and V. I. Klimov, *J. Am. Chem. Soc.*, 2007, **129**, 11708.
40 G. F. Liao, C. X. Li, S. Y. Liu, B. Z. Fang and H. M. Yang, *Trends Chem.*, 2022, **4**, 111.
41 F. He, B. C. Zhu, B. Cheng, J. G. Yu, W. K. Ho and W. Macyk, *Appl. Catal., B*, 2020, **272**, 119006.
42 Q. L. Mo, X. Lin, Z. Q. Wei, X. C. Dai, S. Hou, T. Li and F. X. Xiao, *J. Mater. Chem. A*, 2020, **8**, 16392.
43 A. Alberto, C. Patricia, C. Avelino and G. Hermenegildo, *Angew. Chem., Int. Ed. Engl.*, 2010, **117**, 4134.
44 B. X. Li, T. Gu, T. Ming, J. X. Wang, P. Wang, J. F. Wang and J. C. Yu, *ACS Nano*, 2014, **8**, 8152.
45 L. J. Zhang, S. Li, B. K. Liu, D. J. Wang and T. F. Xie, *ACS Catal.*, 2014, **4**, 3724.
46 B. J. Wallar and J. D. Lipscomb, *Chem. Rev.*, 1996, **96**, 2625.

